Temperature–dependent dynamic plasticity of micro-scale fused silica

Remo N. Widmer, Alexander Groetsch, Guillaume Kermouche, Ana Diaz, Gilles Pillonel, Manish Jain, Rajaprakash Ramachandramoorthy, Laszlo Pethö, Jakob Schwiedrzik, Johann Michler

Materials & Design 215 (2022) 110503

Contents lists available at ScienceDirect

Materials & Design

journal homepage: www.elsevier.com/locate/matdes

Temperature–dependent dynamic plasticity of micro-scale fused silica

Remo N. Widmer [a,d], Alexander Groetsch [a], Guillaume Kermouche [b], Ana Diaz [c], Gilles Pillonel [d], Manish Jain [a], Rajaprakash Ramachandramoorthy [e], Laszlo Pethö [a], Jakob Schwiedrzik [a], Johann Michler [a,*]

[a] Empa - Swiss Federal Laboratories for Materials Science and Technology, Laboratory for Mechanics of Materials & Nanostructures, Feuerwerkerstrasse 39, Thun 3602, Switzerland
[b] Mines Saint-Etienne, Univ Lyon, CNRS, UMR 5307 LGF, Centre SMS, Saint-Etienne, France
[c] Paul Scherrer Institute, Forschungsstrasse 111, Villigen PSI 5232, Switzerland
[d] Alemnis AG, Schorenstrasse 39, Thun 3645, Switzerland
[e] Max-Planck-Institut für Eisenforschung GmbH, Max-Planck-Straße 1, Düsseldorf 40237, Germany

HIGHLIGHTS

- High-temperature micro-compression experiments reveal that the strength of micrometer-sized fused silica drops by approximately 50% at 0.5 T_g.
- The strain rate sensitivity of the yield strength remains low up to 300 °C (≤0.03), but significantly increases at 600 °C (0.09).
- Ptychographic X-ray computed tomography reveals post-compression density distribution with unprecedented spatial resolution (~23 nm^3) and accuracy ($\sigma \sim 0.025$ gm/cm^3)

GRAPHICAL ABSTRACT

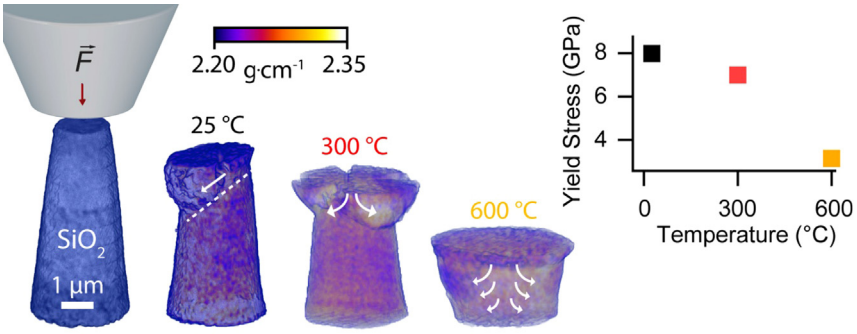

ARTICLE INFO

Article history:
Received 17 December 2021
Revised 25 February 2022
Accepted 28 February 2022
Available online 01 March 2022

Keywords:
Fused silica
Micro-mechanics
Plasticity
High temperature
High strain rate
X-ray ptychographic tomography

ABSTRACT

The ability to predict the micro-scale strength and plasticity of fused-silica micro-components is crucial as their miniaturization and applications in harsh environments advance. This study focusses on the micro-mechanical behavior of fused silica micropillars at high temperatures and variable strain rates. 160 micropillars with a diameter of 1.6 µm have been tested at temperatures between −120 °C and 600 °C and strain rates between 10^{-3} s^{-1} and 1 s^{-1}, which are to date unexplored conditions. Between −120 °C and 300 °C, the yield strengths (6–8 GPa) and strain rate sensitivities (≤0.03) vary only marginally. However, at 600 °C, a significant decrease in yield strength by more than 50 % (2.5–4.5 GPa) and an increase in strain rate sensitivity by a factor of 3 (0.09) is observed. Post-compression synchrotron-based ptychographic X-ray computed tomography (PXCT) on plastically deformed micropillars revealed a transition in deformation mechanisms: Shear-localization and shear-promoted densification at 25 °C; homogeneous shear-flow and densification limited by radial cracking at 300 °C; and unconstrained shear-flow and limited densification due to weak confinement strength at 600 °C. FEM results support these observations while separating geometric from material-intrinsic effects. These results suggest that the classification of fused silica as a glass that deforms predominantly through densification should be challenged – at least under unconstrained compression, which is the predominant mode of loading in applications.

* Corresponding author.
E-mail address: johann.michler@empa.ch (J. Michler).

https://doi.org/10.1016/j.matdes.2022.110503
0264-1275/

1. Introduction

Recent progress in additive manufacturing and laser-based lithography is now enabling the efficient and precise fabrication of complex micrometer-sized glass components [1,2]. The tailorable functional properties of such glasses in combination with their excellent chemical and thermal stability led to myriad technological applications, including in sensors [3], micro-fluidics [4], medical technology [5], data storage [6], and photonics [7]. As the miniaturization of glass components progresses, one begins to encounter important size-effects. Below a certain length scale, the mechanical behavior of microscopic glass parts is no longer predictable based on classical knowledge of bulk-mechanical properties. This is because the probability of occurrence and the size of structural and mechanical flaws decrease together with the tested volume. As a result, the material can now be loaded up to its intrinsic yield strength while averting brittle failure. The threshold size for this transition depends mostly on the specimen preparation technique and has little material-intrinsic significance. In practice it has been shown that for example fused silica fibers can be drawn with diameters up to 80 μm such that their mechanical behavior is independent of their diameter [8]. In the present study, mechanical tests were performed on lithographically fabricated micropillars with diameters of 1.6 μm, as larger diameters would not allow for extended ductile behavior at ambient temperature. The practical relevance of the effect of an increasing strength of fused silica with its miniaturization lies in the enhanced reliability of technological components. Compared to the strength of bulk-sized components (typically around 1–1.5 GPa), μm-sized fused silica can be up to approximately four to six times as strong [9]. Moreover, the glass can subsequently be plastically deformed and intrinsic deformation mechanisms can be observed, based on the atomic interaction only [10].

The three fundamental deformation mechanisms that accommodate plasticity under such conditions are: (1) volume-conservative homogeneous shear flow [11] (2) volume-conservative localized shear banding [12], and (3) non-volume-conservative structural densification. For fused silica, densification saturates at a maximum density of 121 % (approximately 2.66 gm/cm^3) relative to the initial density (approximately 2.20 gm/cm^3) [13]. As temperatures approach the glass transition temperature (approximately 1200 °C), volume-conservative viscous flow presents a fourth mechanism [14]. However, a formal distinction between homogeneous shear flow and viscous flow above the glass transition temperature might not be necessary [15]. The most commonly observed mechanism that accommodates plasticity in fused silica is structural densification. However, the predominance of such structural densification in literature is likely due to the predominance of indentation based mechanical tests.

In micrometer-sized fused silica, all four deformation mechanisms can occur either isolated or combined. The relative contributions depend on external parameters such as the shape of the stress-field, the temperature, or the strain rate, which is equal to the compression speed divided by the initial length. Yet, their interplay remains poorly understood and has still unexpected outcomes [16-22]. Micropillar compression experiments are well-suited for the study of such effects. Typical micropillars with diameters of only a few micrometers down to nanometers fabricated with e.g. focused ion-beam or ion-etching techniques grant sufficiently pristine surfaces to study plasticity beyond the brittle failure due to preexisting flaws. Kermouche et al., for example, have found a homogeneous shear flow dominated response with only a minor contribution of densification and no strain hardening [11]. However, care should be taken to not inflict new influences on the mechanical behavior that stem from the necessary observation techniques. The electron beam from scanning– and transmission electron microscopes for examples is known to facilitate bond breakage and reformation in fused silica, which can significantly soften its mechanical response [23,24]. High temperature and high strain rate testing of such micro pillars has become possible only recently due to progress in instrumentation [12,25,26]. The number of reports on the behavior of fused silica under such extreme conditions is therefore still relatively small. In terms of high strain rates, a strong rate dependence of the deformation mechanism and the maximally achievable plastic strains has been reported from micropillar compression [12]. Using nano-impact testing, a transition has been observed at high strain rates, which was interpreted as a shift from densification-dominated plastic flow to shear-dominated plastic flow [26].

Motivated by the lack of understanding of (1) fundamental properties at high temperatures and (2) the potential adverse effects of operating temperatures and loading conditions on the mechanical performance in applications, the plasticity of fused silica micropillars is explored here by uniaxial compression tests under variable temperatures ranging from −120 °C up to 600 °C and variable strain rate ranging from 0.001 s^{-1} up to 1 s^{-1}. In addition, synchrotron-based ptychographic X-ray computed tomography (PXCT) data is presented on a selected set of deformed micropillars. This technique allowed us to quantify the post-deformation density distribution within the micropillars with the highest accuracy (±5%) and highest spatial resolution (49 nm) for this material to date. Finally, FEM simulations at 25 °C of micropillars compressed to different degrees of strain are presented to separate the effects of temperature and sample geometry.

2. Methods

2.1. Micropillar fabrication

UV-grade fused silica wafers were purchased from Siegert Wafer GmbH, Germany (Table S1). The lithographic procedure for the micropillar fabrication is described in detail in reference [12]. The dissolvable, protective coating with a 14 μm thick photoresist, applied just after fabrication, made sure that the sample experienced no more than 6 h air-exposure during handling prior to the experiments. The sample was tempered in Argon during 12 h at 800 °C. This step was done to ensure that any heating of the sample up to 600 °C for the high-temperature compression tests would not induce any further irreversible tempering during the actual experiment.

2.2. In situ high-temperature tests

In situ high-temperature and low-temperature micropillar compression tests were performed with an Alemnis HTM-1000 and an Alemnis LTM-Cryo installed in a Zeiss DSM 962 scanning electron microscope. The temperature profile of the pre-tempering and high-temperature compression tests is shown in Figure S1. The electron beam was off during all compression tests.

Raw force–displacement curves were corrected by an empirical frame-compliance correction and a theoretical pillar sink-in correction [27], and the initial contact was set to zero strain. Stress–strain curves were then obtained using a top pillar-diameter of 1.64 μm and a pillar height of 5.42 μm. The stress–strain curves recorded at 0.1 s^{-1} and 1 s^{-1} were smoothened to reduce noise and artifacts of resonances.

2.3. X-ray ptychographic computed tomography

Six deformed and two undeformed micropillars were lifted out from the substrate and placed onto two individual OMNY pins [28], which in the following will be referred to as sample 1 and sample 2. The lift-out process involved the following steps: (1) FIB undercutting from two opposite sites at an angle of 35° relative to the substrate surface, while leaving a small strip on one side that still holds the resulting wedge; (2) attaching a micromanipulator needle to the wedge using FIB Pt-deposition; (3) FIB cutting the remaining strip; (4) transferring the micropillar to the OMNY pin; (5) attaching the wedge to the OMNY pin surface by FIB Pt-deposition; (6) FIB cutting micro-manipulator needle. The 3 pillars compressed at a strain rate of 0.001 s^{-1} at temperatures of 25 °C, 300 °C and 600 °C were mounted on sample 1, while the reference uncompressed pillar and the pillar compressed at a strain rate of 1 s^{-1} at 600 °C were mounted on sample 2.

The three-dimensional density distribution of the micropillars was obtained using X-ray ptychographic computed tomography, conducted at the cSAXS beamline of the Swiss Light Source, Paul Scherrer Institute, Switzerland. For the experiments the flOMNI instrument [29] was used, with the specimens mounted in air and at room temperature, and a photon energy of 6.2 keV. A coherently illuminated Fresnel zone plate of 200 μm diameter and 60 nm outer-most zone width was used to define a confined illumination onto the sample with a total flux of about 3×10^8 photons/s. The sample was placed 1.5 mm downstream the focused beam, where the illumination had a size of about 5 μm. The specimens where scanned at positions following a Fermat spiral, and at each position coherent diffraction patterns were recorded with an acquisition time of 0.1 s with an *in vacuo* Eiger 1.5 M detector placed at 5.237 m downstream the specimen. The field of view of the scans covered the entire arrangement of pillars mounted on each pin and was 45 × 12 μm^2 (horizontal × vertical) and 40 × 10 μm^2 with an average step size between the scanning positions of 1 μm and 0.9 μm for sample 1 and sample 2, respectively. Ptychographic reconstructions were performed with the PtychoShelves package [30] using a combination of the difference map [31] algorithm followed by a maximum likelihood algorithm as a refinement. For the reconstructions 400 × 400 pixels of the detector containing the diffraction patterns were selected, resulting in a reconstructed pixel size of 23.27 nm. Ptychographic projections were acquired at 950 and 1000 angular positions equally spaced between 0 and 180° around the vertical axis for samples 1 and 2, respectively. Projections were processed and aligned with subpixel resolution before performing tomographic reconstructions, as described in Ref. [32]. Due to some control issues during the acquisition some projections which could not be reliably recorded were discarded in the tomographic reconstruction, resulting in a total number of projections of 938 and 974 for samples 1 and 2, respectively. Using Fourier shell correlation between 2 subtomograms, each obtained from half of the projections [33], a 3D resolution of 49 nm for sample 1 and 59 nm for sample 2 was estimated. A dose of 2.1×10^8 and 2.6×10^8 is estimated to have been deposited during acquisition on sample 1 and sample 2, respectively, assuming the material composition is SiO_2.

Using Fiji [34], the densities of the tomographic reconstructions were filtered by a threshold of $1.8 < x < 2.4$, to set background pixels and any artefacts from Pt-redeposition to 0. Finally, the images were filtered by a three-dimensional median filter of a radius of 2.

2.4. FEM simulations

Calculations were performed with the finite element software Abaqus, using 3-node linear axisymmetric solid elements CAX3 and a finite transformation formulation based on the multiplicative decomposition of the deformation gradient into an elastic and a plastic part and the Jauman objective stress rate. An implicit FE scheme was used. The flat punch was a rigid body and was pushed vertically to compress the fused silica micropillar. The contact was considered frictionless.

3. Results and discussion

3.1. Micropillar compression

Micropillars with a diameter of 1.60 μm (±0.02 μm), a height of 5.42 μm (±0.01 μm), and a taper angle of 7° (±0.5°) were mass-manufactured using a photolithographic technique described in the literature [12]. The stress–strain curves obtained from a total of 160 compression tests at variable temperature and strain rates contain a number of characteristic features (Fig. 1a, Fig. S2). One of the most direct measures that reflects the distinct temperature– and strain rate dependent mechanical properties is the yield strength (Fig. 1b). This quantity describes the stress at which the transitions from an elastic to a plastic regime and thus the onset of irreversible deformation occurs. The yield strength was defined as the point at which the stress–strain curve deviates from the linear elastic loading segment by 0.2 % strain. This is the most commonly used threshold in a wide range of materials that do not sharply yield [35]. Furthermore, yield strength values were corrected for taper angle that resulted from their fabrication, by using a correction factor of 0.833 [12]. Figs. S3–S18 display the individual stress–strain curves with the corresponding intercepts at 0.02% plastic strain. The yield strength of glass micropillars depends on the testing speed [12]. This can be described by the strain rate sensitivity m, which typically represents a power law relationship between the yield strength and the strain rate. It is defined as $m = d(\ln\sigma)/d(\ln\dot{\varepsilon})$ where σ is the yield strength and $\dot{\varepsilon}$ the strain rate. The temperature-dependent strain rate sensitivity was determined by fitting the coefficients a (intercept) and m (slope) of the function $\ln(\sigma) = a + m * \ln(\dot{\varepsilon})$to our strain rate dependent yield strength data (Fig. 1c, Supplementary Table S2).

At 25 °C and a quasi-static strain rate of 0.001 s^{-1}, a yield strength of approximately 6.7 ± 0.1 GPa is observed, which is in good agreement with independently reported micropillar compression data (*ca.* 6.5–7 GPa) [9,11,36,37]. The strain rate sensitivity at ambient temperature of m = 0.03 ± 0.01, however, is slightly higher than previously published data (m = 0.01) [38]. This difference can be explained based on the fact that Limbach et al. (2014) performed indentation-based strain rate jump tests, whereas in the present study, variable-strain rate uniaxial compression testing was used. The strain rate sensitivity is directly related to the yielding mechanism and the yielding mechanism in glasses, in turn, is highly susceptible to the stress field. As the stress fields are very different in micropillar compression and nano-indentation, different results are to be expected, even if –hypothetically– the material was identical.

From −120 °C up to 25 °C, any variation in yield strength or strain rate sensitivity lies within the standard deviation. In comparison, *in vacuo* variable-temperature tensile strength of pristine fused silica fibers with a diameter of 20–40 μm has also been reported to be insensitive to temperature variations at least within the range from −80 to 200 °C [8] (Fig. 1d). A significant increase in yield strength at lower temperature is only reported at temperatures ≤ −196 °C. The transitional range, however, remains uncharted. Based on our results, this insensitivity appears to extend at least down to −120 °C.

At 300 °C, the effect of temperature on our results is still ambiguous. A significant difference to ambient temperature only becomes visible at intermediate to high strain rates. This trend

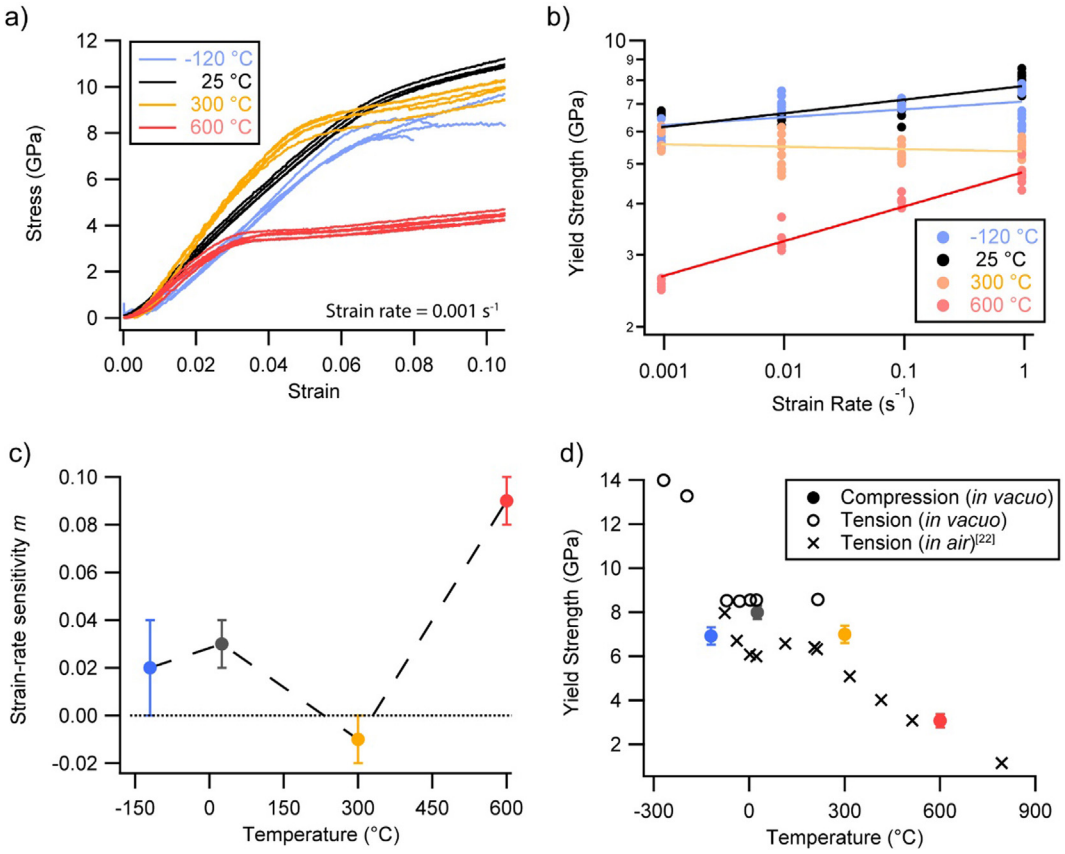

Fig. 1. Micropillar compression data as a function of temperature and strain rate. a) Overview of quasi-static stress–strain curves at variable temperatures (only shown up to a strain of 0.1). Full curves are plotted individually in Figs. S3–S18. b) Strain rate-dependent yield strength at variable temperatures, corrected for tapered pillars by a factor of 0.833 (see section 2.1). c) Temperature-dependent strain rate sensitivity. d) Comparison of temperature-dependent yield strengths from compression (this study) and tension experiments from Proctor et al. (1967) [8].

manifests itself as a net-zero, to slightly negative, strain rate sensitivity of −0.01 ± 0.01. A similar transition to a more pronounced temperature effect above 300 °C occurs under tension in air (Fig. 1d) [8].

Finally, at 600 °C, a substantial drop in yield strength compared to ambient temperatures at all strain rates is observed. The drop in strength from 300 °C to 600 °C is similar in magnitude to that reported under tension in air [8]. Meanwhile, the strain rate sensitivity increases by a factor of 3 to 0.09 ± 0.01, indicating an important change in deformation mechanism.

In summary, there are no clear trends apparent in the yield strength data from −120–300 °C; neither as a function of strain rate at different temperatures, nor as a function of temperature at different strain rates. The first statistically significant trend is a slightly lower strain rate sensitivity at 300 °C compared to −120 °C and 25 °C. Only at 600 °C there is a significant drop in yield strength and a significant increase in strain rate sensitivity compared to 300 °C. This relative insensitivity of fused silica to temperature– and strain rate changes up to 300 °C is also supported in literature data [8]. The reason for the residual scatter of the observed data points around presumed true values is likely due to a statistically limited set of observations.

3.2. Ptychographic X-ray computed tomography

The previous section included a discussion on how temperature and strain rate affect the yield strength. While being an important parameter for basic material characterization as well as engineering tasks, it does not allow for a direct assessment of the underlying yield mechanism nor the subsequent deformation mechanism.

For single- and polycrystalline materials, there are a number of well-established techniques that allow the imaging and quantitative analysis of structural features that accommodate plasticity at the micro- and nano-scale. Transmission electron microscopy (TEM) allows the direct observation of dislocation motion in crystalline lattices, electron- and X-ray diffraction can resolve three-dimensional strain fields, and electron back-scattered diffraction (EBSD) visualizes grain boundary interactions, deformation-twinning, and geometrically necessary dislocation densities. However, none of these techniques is available to study amorphous materials. Finally, while total scattering techniques can be used to infer short-range structural data of glasses, it lacks spatial resolution to resolve features of interest, even if performed at a synchrotron facility.

Several alternative techniques have been proposed for the study of strain in glasses: (1) micro-Raman spectroscopy can be used to reconstruct a density cross-section through a residual Vicker's indent [39]. This technique, however, is limited by a spatial resolution to around 1–3 μm^3 [18]. The inferred densities are not very accurate given the necessity for an empirical Raman shift–density calibration and the generally broad Raman peaks of glasses. (2) Digital holographic tomography (DHT) can help to reconstruct a three-dimensional map of the refractive index around a residual Vicker's indent [40]. The spatial resolution is limited to approximately 0.2 μm. (3) With micro-Brillouin spectroscopy the three-dimensional residual density field of a Vicker's indent can be quantified while lateral and axial resolutions are limited to approxi-

mately 1.2 μm and 6 μm, respectively [41]. Similar to Raman spectroscopy, Brillouin spectroscopy requires an empirical calibration curve. Furthermore, the measured quantity is dependent on both the longitudinal elastic modulus and the density. Inferred densities from this technique therefore contain several assumptions.

Here PXCT [42] was used for the nanoscopic reconstruction of the three-dimensional density distribution of permanently deformed glass micropillars. X-ray ptychography is a high-resolution imaging technique in which coherent diffraction patterns are recorded in the far field from partially overlapping illuminated areas of the sample using a confined, coherent beam [43]. Iterative phase retrieval algorithms are then used to reconstruct the projection of the sample along the X-ray beam direction with both absorption and phase contrast. In ptychography the spatial resolution is only limited by the highest scattering angle that can be reliably measured in the far field and is, thus, not limited by any optics. However, in practice it can be limited by the mechanical stability and accuracy of the sample movements during the scan. X-ray ptychographic phase projections can then be obtained at different incident angles of the beam and combined via conventional tomography to obtain the three-dimensional electron density distribution of the sample with quantitative contrast and a relative error of less than 5 % on each single voxel [44]. Recent developments in instrumentation have shown that PXCT can provide a 3D resolution well below 20 nm on specimens that have sufficiently small features with high density contrast [29]. The PXCT measurements were performed at the cSAXS beamline at the Swiss Light Source, Paul Scherrer Institute, Villigen, Switzerland, as described in the methods section below, where the experimental conditions are optimized for a photon energy of 6.2 keV. One of the advantages to work at this energy is the optimal efficiency of the detector, which is crucial for a reliable measurement of weak signals at high scattering angles, and, thus, crucial for high-resolution imaging. On the other hand, ideally one would like to match the thickness of the sample to the attenuation length of the material to optimize the X-ray scattering signal, but at this energy the X-ray attenuation length of SiO_2 is about 62 μm, much larger than the micropillar thickness. To maximize the efficiency of our PXCT experiment on micropillars of 1.6 μm diameter, a novel strategy was opted where multiple micropillars are imaged simultaneously. In this way diffraction patterns are recorded from several micropillars which were illuminated simultaneously at most of the scanning positions of the sample, in such a way that the scattering signal recorded on the detector extended to higher angles compared to scans in which only one micropillar is illuminated. Tomograms of a total of 8 micropillars were thus obtained based on only two individual measurements. Fig. 2 exemplarily shows the transfer of a single micropillar from the original substrate using FIB-sputtering and FIB-Pt-deposition to an OMNY pin [28], which hosts an ensemble of micropillars.

Fig. 3 shows a volumetric rendering and the density distribution of a generic, undeformed reference micropillar. The maximum of the density distribution lies at 2.196 g/cm^3 (σ = 0.025), which corresponds within a relative error of $\leq$ 0.2 % to the expected density for fused silica of 2.2 g/cm^3. The standard deviation is an upper estimate as determined before any binning [44]. A density profile along the vertical axis after binning of a rectangular region of interest of approximately 0.5x0.5 μm^2 of the micropillar confirms a homogeneous density distribution with a slightly lower mean value of 2.178 g/cm^3. In a first instance, a comparison of the residual pillar shape and density distribution between three individual pillars compressed at 25 °C/0.001 s^{-1}, 300 °C/0.001 s^{-1}, and 600 °C/0.001 s^{-1} (Fig. 4) will be provided.

At 25 °C and 0.001 s^{-1}, a clear-cut shear band inclined by approximately 33° delimits the bottom of a densified zone, as shown in Fig. 4a. The peak density of 2.28 g/cm^3 (+3.8%) drops to the pristine density of 2.19 g/cm^3 within only 110–120 nm normal to the shear-plane. The top-side of the shear-planes, on the other hand, is less-well defined and best described by a gradually increasing density.

A coupling of shear localization and densification has already been investigated by Martinet et al. [20]. The comparison of densification resulting from purely hydrostatic stresses and from both hydrostatic- and shear stresses revealed distinct structural modification. Meanwhile, Kermouche et al. have demonstrated that the load–displacement curves from micro-compression can be satisfactorily modeled with predominant shear flow [11]. Also Ramachandramoorthy et al. [12] argued for a homogeneous flow regime, where shear-transformation zones distribute homogeneously through the bulk of the micropillar, without any contribution from densification. Localized shear-banding was reported only at higher strain rates above 0.07 s^{-1} [12]. Unfortunately, no tomographic data of micropillars compressed at any higher strain rate at 25 °C exists. However, the compression curves at 25 °C look very much alike up to the maximal tested strain rate of 1 s^{-1} (Fig. S19) and display only a minor strain rate sensitivity. No drastic change in deformation mechanism of the present micropillars at strain rates up to 1 s^{-1} is expected.

In contrast to previously reported findings [12] of fused silica micropillar compression tests at 25 °C and strain rates $\geq$ 0.1 s^{-1}, serrated flow as manifested by regularly occurring load-drops during compression is not observed. Yet there is evidence of some extent of strain localization already at low strain rates of 0.001 s^{-1}, as delineated by sharp density contrasts in the tomographic reconstruction (Fig. 4a). Such strain localization can be induced for example by shear softening, however not exclusively [11]. Perfectly plastic flow can, given for instance a non-ideal pillar

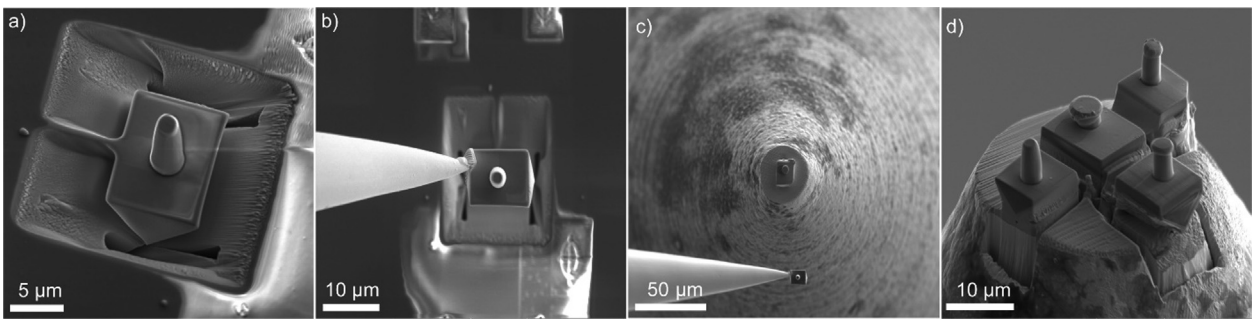

Fig. 2. Overview sample preparation for X-ray ptychographic computed tomography. a) FIB undercut wedge, held on the substrate only by a thin band. b) After attachment of the micromanipulator through Pt deposition, the remaining connection to the substrate is cut. c) transfer of the micropillar to the OMNY pin. d) collection of four micropillars transferred to the OMNY pin and attached through Pt deposition.

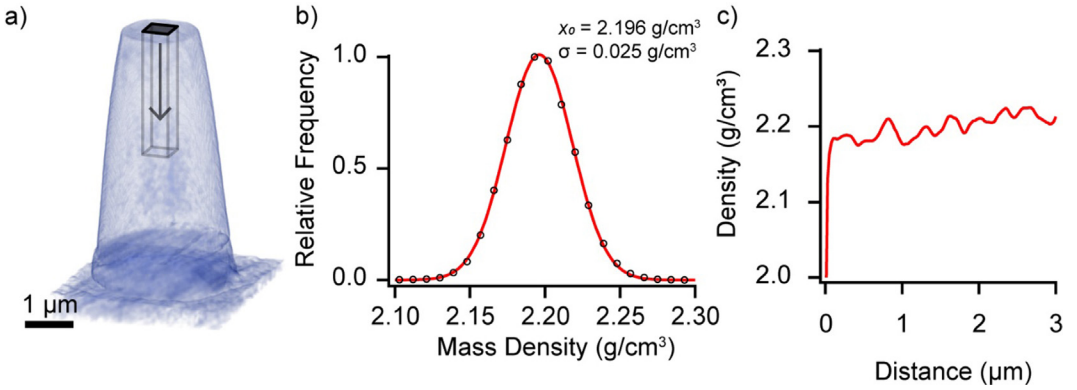

Fig. 3. Tomographic reconstruction of an undeformed fused silica reference micropillar. a) Three-dimensional rendering with an arbitrary transparency setting. b) Histogram of the density distribution of all voxels with a Gaussian fit. The mean value μ corresponds within a relative error of ≤ 0.2 % to the reference density for fused silica of 2.2 g/cm³. The standard deviation before binning amounts to 0.025 g/cm³ c) density profile along the direction of the arrow in a) after two-dimensional binning in the ROI perpendicular to the arrow.

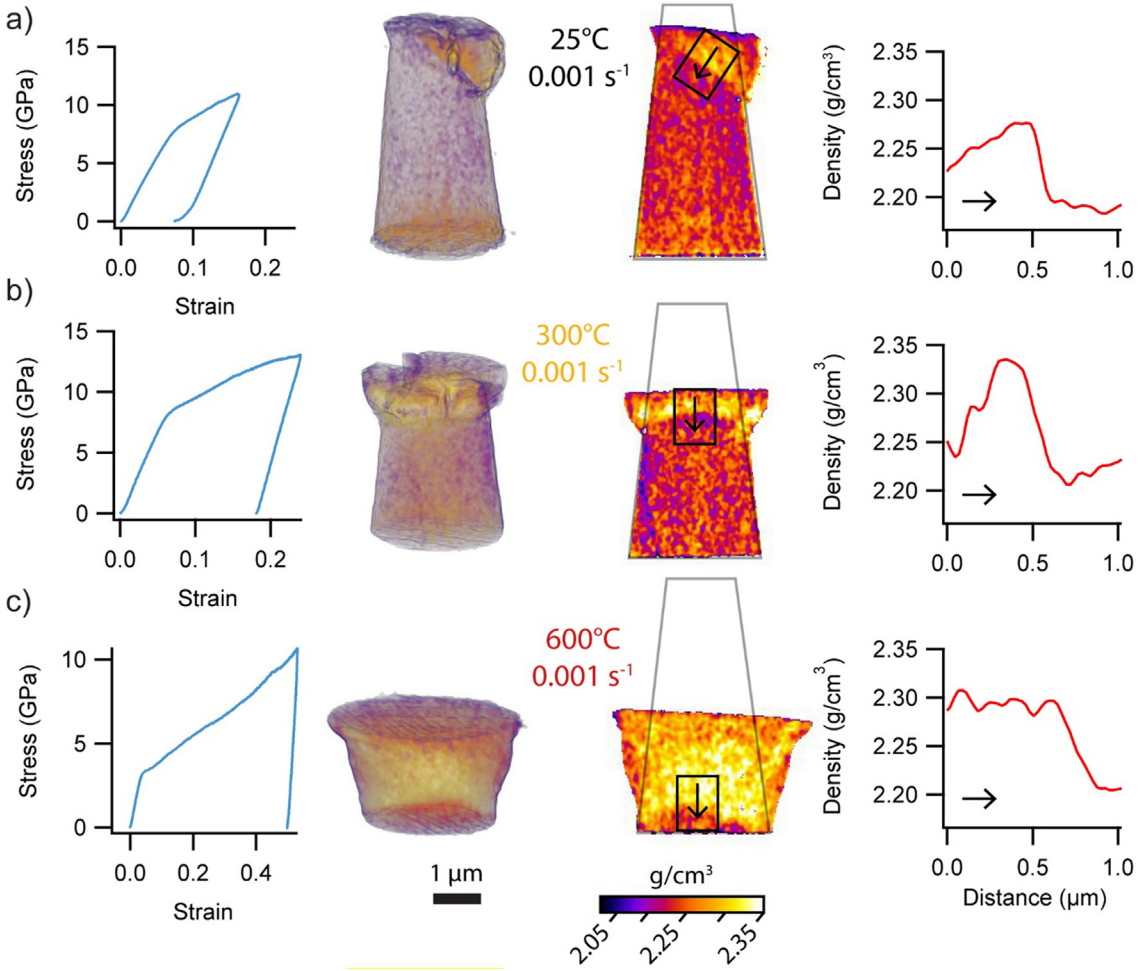

Fig. 4. From left to right: experimental stress–strain curves, volume renderings, two-dimensional slices with the reminiscent shape of the pristine micropillar in the background, and the laterally integrated density profile within the black rectangles. a) 25 °C, 0.001 s^{-1}, b) 300 °C, 0.001 s^{-1}, c) 600 °C, 0.001 s^{-1}. Note that horizontal lines on the top and the bottom of the pillars are measurement artifacts.

geometry, also lead to such strain localization. Based on the present observation only one cannot asses the relative contributions of shear softening and pillar geometry to this strain localization.

On the other hand, it is known that both strain hardening and strain rate sensitivity would prevent from shear localization. Strain hardening increase the yield stress with plastic strain so plastic flow will be distributed. However, fused silica does not show strain hardening [11]. Strain rate sensitivity increases the yield stress with the strain rate. As localization leads to a local increase of the strain rate, materials that are strain rate sensitive are less prone to localization. Fused silica has a relatively low strain rate sensitivity in the strain rate range of question (Fig. 1).

Several reasons can be envisaged that rationalize the difference in the behavior of fused silica as observed in the present study (absence of serrated flow) compared to a previous study [12] (presence of serrated flow). Firstly, the present micropillars were etched using the same protocol, but not on the same fused silica raw material quality. Small changes in for example the OH content can drastically change thermal and mechanical behavior of bulk material. UV–grade fused silica containing 1100–1300 ppm OH has a strain–, softening–, and annealing point reduced by 200 °C compared to full spectrum grade fused silica with less than 10 ppm of OH (Table S2). Secondly, the micropillars in the previous study were tested without any additional annealing, whereas the present micropillars were annealed during 12 h at 800 °C prior to compression testing. It is currently unclear what influence this heat-treatment can have. However, it has been reported that different gases and process parameters during reactive ion etching of fused silica can significantly influence the surface roughness and the chemical composition of the surface layer [45,46].

At 300 °C and 0.001 s^{-1} the compressed micropillar shows no discernible shear-plane anymore. The geometric extent of the densified zone is best described by a convex cap shape. The density of this cap increases gradually and almost symmetrically from the bottom and from the top in axial directions over approximately 350 nm to reach the peak density of 2.34 g/cm^3 (+6.6% standard fused silica). In addition to the densification, there is also clear evidence for homogeneous shear-flow. This becomes apparent when comparing the outer shape of the deformed micropillar with that of an undeformed micropillar. The shear flow is accompanied by radial cracks due to tensile stress in the periphery of the micropillar. As explained by Kermouche et al. [11], this radial cracking is not expected for pure uniaxial compression and is likely caused by the non-ideal shape of the micropillars. Unfortunately, the resolution of the tomographic data in combination with problematic artefacts that occur right at the interface of two media with significantly different densities (in this case air and fused silica) prevents from a meaningful analysis of the local crack environment.

At 600 °C and 0.001 s^{-1}, the material becomes fully plastic through pervasive densification and homogeneous shear-flow. Furthermore, no radial cracks are observed, likely because the material is now too soft to build up tensile stress high enough to initiate radial cracking. As a further result of this softening, the peak density reaches only 2.32 g/cm^3 (+5.6% compared to standard fused silica), which is slightly lower than that obtained at 300 °C.

No change in the deformation mechanism at 600 °C was observed when comparing the two strain rates of 0.001 s^{-1} and 1 s^{-1}, except for a slight increase in the hardening rate. At both strain rates, a very similar density distribution, post-deformation shape, and maximum density of 2.34–2.35 g/cm^3 is obtained (Fig. 5a).

The degree of densification of fused silica under hot-hydrostatic compression as a function of temperature and hydrostatic pressure (compiled by Guerette et al. [47]) is shown in Fig. 5b. For comparison, the maximally obtained density versus maximal flow stress from our three quasi-static compression experiments at 25°, 300 °C, and 600 °C was added. Here, the maximal flow stress was calculated based on the maximal load at maximal strain and the final cross-section area at the top of the deformed micropillars. One should highlight that this comparison is of qualitative nature. However, it highlights well the effect of shear stress on densification. It appears that the same degree of densification can be achieved under uniaxial compression and under hydrostatic compression, though at roughly 300–400 °C lower temperatures in the uniaxial case. This is probably the result of an effect of shear-promoted densification, first noted by Mackenzie (1963) [48]. The maximum degree of densification that can be obtained under uniaxial compression, on the other hand, remains relatively limited due to the lack of confining pressure and consequently favored deformation via shear flow [37].

3.3. FEM simulations

FEM simulations were performed in order to differentiate the effects of temperature and increasing plastic strain, and to compare the experimentally observed degree of densification with theoretically expected values. The mechanical properties of fused silica were simulated using an elliptic model [16,37] that allows for densification up to saturation. The detailed description of the used cap model for fused silica at ambient temperature and the constitutive parameters can be found elsewhere [16]. This constitutive model has previously been used to successfully reproduce indentation-induced densification as well as micropillar compression curves [11,49]. Only simulation at ambient temperatures were performed because the constitutive model parameters for different temperatures are not yet known.

Fig. 6 shows the principal stress field, the plastic strain, and the density at three distinct points of deformation. The progressive strain steps correspond to (1) the strain at which the shear band is nucleated at 25 °C, $\varepsilon = 0.18$; (2) the strain at which radial cracking is observed at 300 °C, $\varepsilon = 0.24$; and (3) the maximum strain applied at 600 °C, $\varepsilon = 0.54$. Fig. S20 provides the comparison of the load displacement curve at RT and Supplementary Videos 1–3 the animated data.

The FEM results show that the principal stress field and the plastic strain is heterogeneous, progressing from the top to the bottom of the pillar. This is likely a consequence of the relatively high taper angle of approximately 7°. Meanwhile, the densification remains low during the whole compression process, which is consistent with previous observations made on different fused silica micropillars [11]. For the largest part, the maximal density does not exceed 2.30 g/cm^3, irrespective of the applied strain, which is in excellent agreement with the experimental tomographic observations.

The experimentally observed shear-band nucleation site corresponds to the region where densification and plastic strain gradients are at their maximum (Fig. 5a). This localization is likely a consequence of the upper part of the pillar that undergoes plastic flow by expanding radially while being constrained by the lower part. Such a phenomenon is enhanced by the taper angle. At a given point, a shear band can be nucleated at the intersection between the upper part and the lower part if shear flow is prone to localize, which is what likely happened at ambient temperature. There might be an interaction between densification and shear localization since densification decreases the yield stress for specific stress states [50]. If shear localization does not occur, pillar compression can continue until the principal stress at the top periphery reaches the crack threshold, *i.e.* a stress state were the radial tensile stress component exceeds the material's strength (Fig. 5b). This is likely what was observed experimentally at 300 °C. Such crack patterns, *i.e.* regularly spaced radial cracks at the periphery (Fig. 4b), were already observed by Lacroix et al. [37]. Finally, if the principal stress never reaches the crack threshold then compression can continue up to a very large compression strain (Fig. 5c). This is likely what was observed experimentally at 600 °C, where the yield and flow stress was much lower than the crack threshold. However, one cannot directly compare our high temperature experiments with modelling because there is currently no constitutive parameters available for the behavior of fused silica at high temperatures. Nevertheless, a good agreement was found in terms of residual shape between numerical results using a room temperature constitutive parameters and experimental results at temperatures up to 600 °C. This means that the constitutive model should be able to reproduce plastic flow of silica at

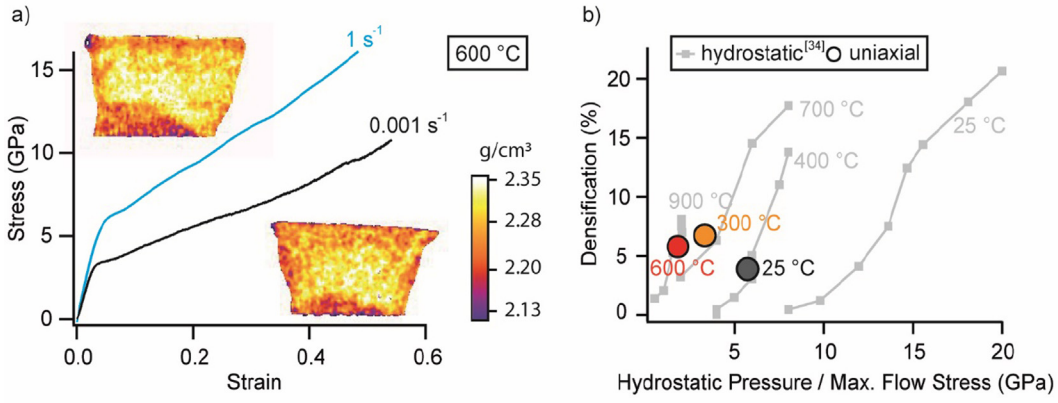

Fig. 5. a) Central slices of tomographic reconstructions and corresponding stress–strain curves of uniaxially compression fused silica micropillars at 600 °C at 0.001 s^{-1} (raw) and 1 s^{-1} (smoothed). b) Densification–pressure–temperature relationship from hot-hydrostatic compression (compiled by Guerette et al. [47]) compared to the maximum flow stress of uniaxial compression from the present work.

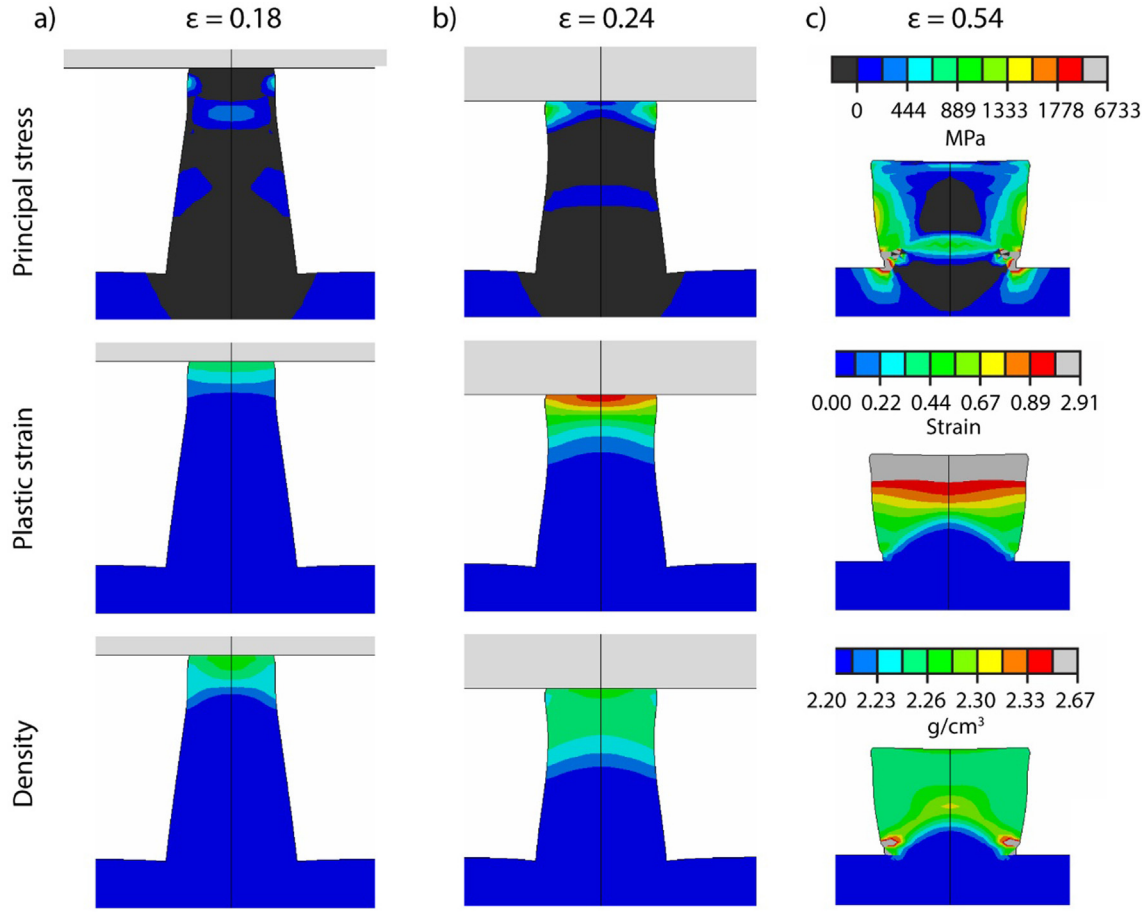

Fig. 6. Evolution of principal stress, plastic strain and density during fused silica micropillar compression at 25 °C using an elliptic constitutive model [37]. a) strain for which the shear band is initiated at 25 °C. b) strain for which top surface radial cracking is observed experimentally at 300 °C. c) residual pillar shape after compression up to the maximum strain at 600 °C. Color scales for stress, strain, and density are identical for a)-c), respectively.

a high temperature, which should be the goal of a future work. As an approximation to the full modelling of the behavior at 600 °C, the behavior of an equivalent pillar but with a yield stress of only 3.5 GPa was tested (Fig. S21). The result shows that decreasing the yield stress down to 3.5 GPa (50% of the yield stress at room temperature) also decreases the maximum tensile stress by about 50%. The pillars shape is only slightly affected due to the lower elastic strain at yielding.

The density does not exceed 2.3 g/cm^3 for most of the residual pillars, except for some very small and localized regions, which is still significantly below the maximal possible densification of approximately 2.66 g/cm^3. A high density gradient is observed in both the experimental and numerical results, especially along the vertical axis. A sharp evolution from 2.3 g/cm^3 to 2.2 g/cm^3 (initial density) can be noted when approaching the pillar's lower part, reflecting a heterogeneous stress field.

In summary, our FEM simulations underline that the tapered shape of pillars induce a gradient of plastic strain in the pillar that can lead to localization events if fused silica is prone to strain softening. Furthermore, it showed that the crack threshold is not reached during compression likely due to lowering of the flow stress with increasing temperature. Finally, our calculations confirm that densification does occur, however, only to a relatively small extent in view of the extreme plastic strain that was achieved. Similar conclusions have been reported recently for nano-indentation, where it was shown that shear flow was the dominant mechanism controlling indentation cracking, whereas densification did not play an important role [51].

3.4. Atomistic description of shear flow in fused silica

In the previous sections, the experimental and calculated evidence for a dominant role of homogeneous shear flow in fused silica under uniaxial compression was detailed, which is also in line with previous literature. Naturally, the question arises what the underlying atomistic mechanism is that allows for such shear flow. In the following the current opinions on this topic are briefly reviewed.

Similar to the mechanism of pure densification up to pressures of 20 GPa, the geometry of individual SiO_4 tetrahedra during shear deformation is assumed to remain rigid [52-54]. The medium-range glass network, on the other hand, is generally believed to undergo an overall decrease in ring-size during shearing [20,55,56]. An alternative theory also describes the local formation of considerably larger rings (“nano-voids”) [57-60]. These voids result from sequential Si—O bond rupture and coalesce almost instantaneously. Such individual shear events correlate with continuously occurring abrupt stress drops in calculated stress–strain curves. Importantly, these stress drops are not be confused with the experimentally observed stress drops during deformation of bulk samples [12]. The simulations concern atomic-scale model-structures with a high sensitivity for individual topological changes [61]. Stress drops observed during macroscopic deformation of bulk fused silica, on the other hand, correspond to shear band propagations or possibly micro-crack propagations. Experimentally, Huang et al. [62] captured atomic resolution TEM images of two-dimensional fused silica and reported the direct observation of ring rearrangements in a sample under shear stress. Overall ring-size reduction and/or the formation of nano-voids are thus thought of as the two main mechanisms during shear deformation. Either mechanism requires the breaking and reformation of bonds. Nucleation points with an increased reactivity of bonding sites that have been proposed are five-fold coordinated Si [55] and under-coordinated Si and non-bridging O [56].

Finally, from the point of view of a super-cooled liquid that approaches its glass transition temperature, it is clear that the viscosity and shear flow properties are directly related to the energy that is required to break and reform the covalent Si–O bonds. A mechanistic picture of such viscous flow was suggested in which threefold-coordinated Si and non-bridging O act as thermally activated, mobile point defects that move through bond-switching processes [14,63]. If one were to extrapolate such mechanisms and their energy barriers to temperatures significantly below the glass transition temperature T_g (e.g. 0.5 T_g as in the present study), only very little softening would be expected because of the exponential relationship of temperature and viscosity [64].

4. Conclusion

The influence of temperature and strain rate on the strength and plasticity of fused silica micropillars was investigated. To this end, *in situ* variable-strain rate and variable–temperature compression experiments were performed. Furthermore, a subset of the deformed micropillars using X-ray Ptychographic computed tomography was imaged – to our knowledge the first use of this technique on the topic of plasticity of glasses. Finally, the deformation was simulated by FEM. The mechanical behavior is characterized by a non-linear temperature dependence of the absolute yield strength and of the strain rate sensitivities of the yield strength. From −120 °C up to 300 °C, the yield strength and strain rate sensitivities varied only marginally at quasi-static strain rates and slightly more pronounced at higher strain rates. At 600 °C, in contrast, a significant decrease in yield strength, accompanied by an increase in strain rate sensitivity was observed. The corresponding deformation mechanisms at quasi-static strain rates are convoluted in a complex fashion: Temperature-dependent propensity for densification, temperature-dependent softening, and geometry-dependent stress-localization. 25 °C: shear-localization due to geometry-induced stress concentration, accompanied by shear-promoted local densification. 300 °C: homogeneous shear-flow and densification, both limited by radial cracking. 600 °C: unconstrained shear-flow and densification, the latter limited due to weak confinement strength. The maximal density obtained under hot-uniaxial compression amounted to 2.34 g/cm^3 at 300 °C, which corresponds to a densification of + 6.6% relative to pristine fused silica.

Our FEM simulations indicated that the formation of a localized shear band may not necessarily be an intrinsic deformation mechanism but rather an effect of the pillar geometry that leads to stress concentrations. Furthermore, our FEM simulations also supports the finding of a shear-flow dominated behavior with only a relatively small degree of densification at 25 °C, which supports previous findings from previous literature.

Overall, these results provide a new perspective on the interplay of various deformation mechanisms that accommodate plasticity in fused silica and their temperature-dependence. Particularly salient appears the softening that leads to unconfined shear flow at temperatures as low as 0.5 T_g. While miniaturization does lead to increased strength compared to bulk sizes, it is crucial to realize that softening of the material due to increased temperature will be pronounced already much below the glass transition temperature.

Importantly the use of X-ray ptychographic computed tomography was introduced, a technique that now matches the required contrast and spatial resolution to investigate plasticity-enabling mechanisms in amorphous materials. Future directions on this topic should be directed towards very high strain rate compression at high-temperature to investigate molecular mechanisms of plasticity based on their kinetic response. Also a better temperature resolution would be desirable in order to pinpoint exact transition points. Finally, care has to be taken in order to distinguish intrinsic material properties from artifacts from sample manufacturing. In the case of glasses, this extends to the thermal history of the samples as these materials, by definition, are never in an energetic equilibrium.

Declaration of Competing Interest

The authors declare that they have no known competing financial interests or personal relationships that could have appeared to influence the work reported in this paper.

Acknowledgements

R.N.W. acknowledges funding from the EMPAPOSTDOCS-II program, which received funding from the European Union’s Horizon 2020 research and innovation program under the Marie

Skłodowska-Curie grant agreement number 754364. We acknowledge the Paul Scherrer Institut, Villigen, Switzerland for provision of synchrotron radiation beamtime at the cSAXS beamline of the Swiss Light Source, Paul Scherrer Institute, Villigen, Switzerland. Finally, we also thank Manuel Guizar-Sicairos and Mirko Holler for important discussions regarding sample preparation.

Data availability

Mechanical data will be available upon request. Tomographic data can be retrieved from https://doi.org/10.16907/5b556500-3577-4f16-94aa-dadf33ac87bd.

Appendix A. Supplementary material

Supplementary data to this article can be found online at https://doi.org/10.1016/j.matdes.2022.110503.

References

[1] F. Kotz, K. Arnold, W. Bauer, D. Schild, N. Keller, K. Sachsenheimer, T.M. Nargang, C. Richter, D. Helmer, B.E. Rapp, Three-dimensional printing of transparent fused silica glass, Nature 544 (7650) (2017) 337–339, https://doi.org/10.1038/nature22061.
[2] D.G. Moore, L. Barbera, K. Masania, A.R. Studart, Three-dimensional printing of multicomponent glasses using phase-separating resins, Nat. Mater. 19 (2) (2020) 212–217, https://doi.org/10.1038/s41563-019-0525-y.
[3] B.o. Lenssen, Y. Bellouard, Optically transparent glass micro-actuator fabricated by femtosecond laser exposure and chemical etching, Appl. Phys. Lett. 101 (10) (2012) 103503, https://doi.org/10.1063/1.475023610.1063/1.4750236.1.
[4] K.S. Elvira, X.C. i Solvas, R.C.R. Wootton, A.J. deMello, The past, present and potential for microfluidic reactor technology in chemical synthesis, Nat. Chem. 5 (11) (2013) 905–915, https://doi.org/10.1038/nchem.1753.
[5] L. Gervais, N. de Rooij, E. Delamarche, Microfluidic Chips for Point-of-Care Immunodiagnostics, Adv. Mater. 23 (24) (2011) H151–H176, https://doi.org/10.1002/adma.201100464.
[6] J. Zhang, M. Gecevičius, M. Beresna, P.G. Kazansky, Seemingly Unlimited Lifetime Data Storage in Nanostructured Glass, Phys. Rev. Lett. 112 (2014), https://doi.org/10.1103/PhysRevLett.112.033901 033901.
[7] H.-K. Choi, M.S. Ahsan, D. Yoo, I.-B. Sohn, Y.-C. Noh, J.T. Kim, D. Jung, J.H. Kim, Formation of cylindrical micro-lens array in fused silica glass using laser irradiations, in: J. Friend, H.H. Tan (Eds.), Micro/Nano Mater. Devices, Syst, International Society for Optics and Photonics, 2013, p. 89234T, https://doi.org/10.1117/12.2033772.
[8] B.A. Proctor, I. Whitney, J.W. Johnson, The strength of fused silica, Proc. R. Soc. London. Ser. A. Math. Phys. Sci. 297 (1967) 534–557, https://doi.org/10.1098/rspa.1967.0085.
[9] R.N. Widmer, D. Bischof, J. Jurczyk, M. Michler, J. Schwiedrzik, J. Michler, Smooth or not: Robust fused silica micro-components by femtosecond-laser-assisted etching, Mater. Des. 204 (2021) 109670, https://doi.org/10.1016/j.matdes.2021.109670.
[10] C.R. Kurkjian, P.K. Gupta, R.K. Brow, The Strength of Silicate Glasses: What Do We Know, What Do We Need to Know?, Int J. Appl. Glas. Sci. 1 (2010) 27–37, https://doi.org/10.1111/j.2041-1294.2010.00005.x.
[11] G. Kermouche, G. Guillonneau, J. Michler, J. Teisseire, E. Barthel, Perfectly plastic flow in silica glass, Acta Mater. 114 (2016) 146–153, https://doi.org/10.1016/J.ACTAMAT.2016.05.027.
[12] R. Ramachandramoorthy, J. Schwiedrzik, L. Petho, C. Guerra-Nunez, D. Frey, J. M. Breguet, J. Michler, Dynamic Plasticity and Failure of Microscale Glass: Rate-Dependent Ductile-Brittle-Ductile Transition, Nano Lett. 19 (2019) 2350–2359, https://doi.org/10.1021/acs.nanolett.8b05024.
[13] S. Romeis, J. Paul, P. Herre, D. de Ligny, J. Schmidt, W. Peukert, Local densification of a single micron sized silica sphere by uniaxial compression, Scr. Mater. 108 (2015) 84–87, https://doi.org/10.1016/j.scriptamat.2015.06.023.
[14] N.F. Mott, The viscosity of vitreous silicon dioxide, Philos. Mag. B. 56 (2) (1987) 257–262.
[15] F. Spaepen, A microscopic mechanism for steady state inhomogeneous flow in metallic glasses, Acta Metall. 25 (1977) 407–415, https://doi.org/10.1016/0001-6160(77)90232-2.
[16] S. Bruns, T. Uesbeck, S. Fuhrmann, M. Tarragó Aymerich, L. Wondraczek, D. Ligny, K. Durst, Indentation densification of fused silica assessed by raman spectroscopy and constitutive finite element analysis, J. Am. Ceram. Soc. 103 (5) (2020) 3076–3088.
[17] T. Vo, B. Reeder, A. Damone, P. Newell, Effect of Domain Size, Boundary, and Loading Conditions on Mechanical Properties of Amorphous Silica: A Reactive Molecular Dynamics Study, Nanomaterials 10 (2020) 54.
[18] Y.B. Gerbig, C.A. Michaels, In-situ Raman spectroscopic measurements of the deformation region in indented glasses, J. Non. Cryst. Solids. 530 (2020) 119828, https://doi.org/10.1016/j.jnoncrysol.2019.119828.
[19] W. Schill, J.P. Mendez, L. Stainier, M. Ortiz, Shear localization as a mesoscopic stress-relaxation mechanism in fused silica glass at high strain rates, J. Mech. Phys. Solids. 140 (2020), https://doi.org/10.1016/j.jmps.2020.103940 103940.
[20] C. Martinet, M. Heili, V. Martinez, G. Kermouche, G. Molnar, N. Shcheblanov, E. Barthel, A. Tanguy, Highlighting the impact of shear strain on the SiO2 glass structure: From experiments to atomistic simulations, J. Non. Cryst. Solids. 533 (2020) 119898, https://doi.org/10.1016/j.jnoncrysol.2020.119898.
[21] O. Benzine, S. Bruns, Z. Pan, K. Durst, L. Wondraczek, Local Deformation of Glasses is Mediated by Rigidity Fluctuation on Nanometer Scale, Adv. Sci. 5 (2018) 1800916, https://doi.org/10.1002/advs.201800916.
[22] A. Groetsch, A. Gourrier, J. Schwiedrzik, M. Sztucki, R.J. Beck, J.D. Shephard, J. Michler, P.K. Zysset, U. Wolfram, Compressive behaviour of uniaxially aligned individual mineralised collagen fibres at the micro- and nanoscale, Acta Biomater. 89 (2019) 313–329, https://doi.org/10.1016/j.actbio.2019.02.053.
[23] P.M. Ajayan, S. Iijima, Electron-beam-enhanced flow and instability in amorphous silica fibres and tips, Philos. Mag. Lett. 65 (1) (1992) 43–48, https://doi.org/10.1080/09500839208215146.
[24] K. Zheng, C. Wang, Y.-Q. Cheng, Y. Yue, X. Han, Z. Zhang, Z. Shan, S.X. Mao, M. Ye, Y. Yin, E. Ma, Electron-beam-assisted superplastic shaping of nanoscale amorphous silica, Nat. Commun. 1 (2010) 24, https://doi.org/10.1038/ncomms1021.
[25] J.M. Wheeler, J. Michler, Elevated temperature, nano-mechanical testing in situ in the scanning electron microscope, Rev. Sci. Instrum. 84 (4) (2013) 045103, https://doi.org/10.1063/1.4795829.
[26] C. Zehnder, J.-N. Peltzer, J.-S.-K.-L. Gibson, S. Korte-Kerzel, High strain rate testing at the nano-scale: A proposed methodology for impact nanoindentation, Mater. Des. 151 (2018) 17–28, https://doi.org/10.1016/j.matdes.2018.04.045.
[27] H. Zhang, B.E. Schuster, Q. Wei, K.T. Ramesh, The design of accurate micro-compression experiments, Scr. Mater. 54 (2) (2006) 181–186, https://doi.org/10.1016/j.scriptamat.2005.06.043.
[28] M. Holler, J. Raabe, R. Wepf, S.H. Shahmoradian, A. Diaz, B. Sarafimov, T. Lachat, H. Walther, M. Vitins, OMNY PIN - A versatile sample holder for tomographic measurements at room and cryogenic temperatures, Rev. Sci. Instrum. 88 (11) (2017) 113701, https://doi.org/10.1063/1.4996092.
[29] M. Holler, A. Diaz, M. Guizar-Sicairos, P. Karvinen, E. Färm, E. Härkönen, M. Ritala, A. Menzel, J. Raabe, O. Bunk, X-ray ptychographic computed tomography at 16 nm isotropic 3D resolution, Sci. Rep. 4 (2014) 3857, https://doi.org/10.1038/srep03857.
[30] K. Wakonig, H.-C. Stadler, M. Odstrčil, E.H.R. Tsai, A. Diaz, M. Holler, I. Usov, J. Raabe, A. Menzel, M. Guizar-Sicairos, PtychoShelves, a versatile high-level framework for high-performance analysis of ptychographic data, J. Appl. Crystallogr. 53 (2) (2020) 574–586, https://doi.org/10.1107/S1600576720001776.
[31] P. Thibault, M. Dierolf, O. Bunk, A. Menzel, F. Pfeiffer, Probe retrieval in ptychographic coherent diffractive imaging, Ultramicroscopy. 109 (4) (2009) 338–343, https://doi.org/10.1016/j.ultramic.2008.12.011.
[32] M. Odstrčil, M. Holler, J. Raabe, M. Guizar-Sicairos, Alignment methods for nanotomography with deep subpixel accuracy, Opt. Express. 27 (25) (2019) 36637, https://doi.org/10.1364/OE.27.036637.
[33] M. van Heel, M. Schatz, Fourier shell correlation threshold criteria, J. Struct. Biol. 151 (3) (2005) 250–262.
[34] J. Schindelin, I. Arganda-Carreras, E. Frise, V. Kaynig, M. Longair, T. Pietzsch, S. Preibisch, C. Rueden, S. Saalfeld, B. Schmid, J.-Y. Tinevez, D.J. White, V. Hartenstein, K. Eliceiri, P. Tomancak, A. Cardona, Fiji: an open-source platform for biological-image analysis, Nat. Methods. 9 (7) (2012) 676–682, https://doi.org/10.1038/nmeth.2019.
[35] J.M.R. Conrad Paulson Scott K. Graham, and David Darwin, Defining Yield Strength for Nonprestressed Reinforcing Steel, ACI Struct. J. 113 (n.d.). https://doi.org/10.14359/51688199.
[36] S.M. Han, C. Xie, Y. Cui, Microcompression of fused silica nanopillars synthesized using reactive ion etching, Nanosci. Nanotechnol. Lett. 2 (2010) 344–347, https://doi.org/10.1166/nnl.2010.1105.
[37] R. Lacroix, G. Kermouche, J. Teisseire, E. Barthel, Plastic deformation and residual stresses in amorphous silica pillars under uniaxial loading, Acta Mater. 60 (15) (2012) 5555–5566.
[38] R. Limbach, B.P. Rodrigues, L. Wondraczek, Strain-rate sensitivity of glasses, J. Non. Cryst. Solids. 404 (2014) 124–134, https://doi.org/10.1016/j.jnoncrysol.2014.08.023.
[39] A. Perriot, D. Vandembroucq, E. Barthel, V. Martinez, L. Grosvalet, C.h. Martinet, B. Champagnon, Raman Microspectroscopic Characterization of Amorphous Silica Plastic Behavior, J. Am. Ceram. Soc. 89 (2) (2006) 596–601, https://doi.org/10.1111/j.1551-2916.2005.00747.x.
[40] Y. Sung, S. Yoshida, Y. Kato, C. Kurkjian, Three-dimensional densification measurement of Vickers-indented glass using digital holographic tomography, J. Am. Ceram. Soc. 102 (10) (2019) 5866–5872.
[41] H. Tran, S. Clément, R. Vialla, D. Vandembroucq, B. Rufflé, Micro-Brillouin spectroscopy mapping of the residual density field induced by Vickers indentation in a soda-lime silicate glass, Appl. Phys. Lett. 100 (23) (2012) 231901, https://doi.org/10.1063/1.4725488.
[42] M. Dierolf, A. Menzel, P. Thibault, P. Schneider, C.M. Kewish, R. Wepf, O. Bunk, F. Pfeiffer, Ptychographic X-ray computed tomography at the nanoscale, Nature. 467 (7314) (2010) 436–439, https://doi.org/10.1038/nature09419.

[43] F. Pfeiffer, X-ray ptychography, Nat. Photonics. 12 (1) (2018) 9–17, https://doi.org/10.1038/s41566-017-0072-5.
[44] A. Diaz, P. Trtik, M. Guizar-Sicairos, A. Menzel, P. Thibault, O. Bunk, Quantitative x-ray phase nanotomography, Phys. Rev. B - Condens. Matter Mater. Phys. 85 (2012), https://doi.org/10.1103/PhysRevB.85.020104 020104.
[45] L. Sun, H. Jin, X. Ye, H. Liu, F. Wang, X. Jiang, W. Wu, W. Zheng, Surface modification and etch process optimization of fused silica during reaction CHF3-Ar plasma etching, Optik (Stuttg). 127 (1) (2016) 206–211, https://doi.org/10.1016/j.ijleo.2015.10.046.
[46] H. Jin, Q. Xin, N. Li, J. Jin, B. Wang, Y. Yao, The morphology and chemistry evolution of fused silica surface after Ar/CF 4 atmospheric pressure plasma processing, Appl. Surf. Sci. 286 (2013) 405–411, https://doi.org/10.1016/j.apsusc.2013.09.100.
[47] M. Guerette, M.R. Ackerson, J. Thomas, F. Yuan, E. Bruce Watson, D. Walker, L. Huang, Structure and Properties of Silica Glass Densified in Cold Compression and Hot Compression, Sci. Rep. 5 (2015) 15343, https://doi.org/10.1038/srep15343.
[48] J.D. Mackenzie, High-Pressure Effects on Oxide Glasses: I, Densification in Rigid State, J. Am. Ceram. Soc. 46 (10) (1963) 461–470, https://doi.org/10.1111/j.1151-2916.1963.tb13776.x.
[49] G. Kermouche, E. Barthel, D. Vandembroucq, P.h. Dubujet, Mechanical modelling of indentation-induced densification in amorphous silica, Acta Mater. 56 (13) (2008) 3222–3228.
[50] G. Molnár, G. Kermouche, E. Barthel, Plastic response of amorphous silicates, from atomistic simulations to experiments – A general constitutive relation, Mech. Mater. 114 (2017) 1–8, https://doi.org/10.1016/j.mechmat.2017.07.002.
[51] E. Barthel, V. Keryvin, G. Rosales-Sosa, G. Kermouche, Indentation cracking in silicate glasses is directed by shear flow, not by densification, Acta Mater. 194 (2020) 473–481, https://doi.org/10.1016/j.actamat.2020.05.011.
[52] A. Zeidler, K. Wezka, R.F. Rowlands, D.A.J. Whittaker, P.S. Salmon, A. Polidori, J. W.E. Drewitt, S. Klotz, H.E. Fischer, M.C. Wilding, C.L. Bull, M.G. Tucker, M. Wilson, High-Pressure Transformation of SiO2 Glass from a Tetrahedral to an Octahedral Network: A Joint Approach Using Neutron Diffraction and Molecular Dynamics, Phys. Rev. Lett. 113 (2014), https://doi.org/10.1103/PhysRevLett.113.135501 135501.
[53] T. Sato, N. Funamori, High-pressure structural transformation of SiO2 glass up to 100 GPa, Phys. Rev. B. 82 (2010), https://doi.org/10.1103/PhysRevB.82.184102 184102.
[54] B. Mantisi, G. Kermouche, E. Barthel, A. Tanguy, Impact of pressure on plastic yield in amorphous solids with open structure, Phys. Rev. E. 93 (2016) 33001, https://doi.org/10.1103/PhysRevE.93.033001.
[55] N.S. Shcheblanov, B. Mantisi, P. Umari, A. Tanguy, Detailed analysis of plastic shear in the Raman spectra of SiO2 glass, J. Non. Cryst. Solids. 428 (2015) 6–19, https://doi.org/10.1016/J.JNONCRYSOL.2015.07.035.
[56] K.-I. Nomura, Y.-C. Chen, R.K. Kalia, A. Nakano, P. Vashishta, Defect migration and recombination in nanoindentation of silica glass, Appl. Phys. Lett. 99 (11) (2011) 111906, https://doi.org/10.1063/1.3637052.
[57] F. Bamer, F. Ebrahem, B. Markert, Elementary plastic events in a Zachariasen glass under shear and pressure, Materialia. 9 (2020) 100556, https://doi.org/10.1016/j.mtla.2019.100556.
[58] Y.-C. Chen, Z. Lu, K. Nomura, W. Wang, R.K. Kalia, A. Nakano, P. Vashishta, Interaction of Voids and Nanoductility in Silica Glass, Phys. Rev. Lett. 99 (2007), https://doi.org/10.1103/PhysRevLett.99.155506 155506.
[59] A. Pedone, G. Malavasi, M.C. Menziani, U. Segre, A.N. Cormack, Molecular Dynamics Studies of Stress−Strain Behavior of Silica Glass under a Tensile Load, Chem. Mater. 20 (13) (2008) 4356–4366, https://doi.org/10.1021/cm800413v.
[60] J. Luo, J. Wang, E. Bitzek, J.Y. Huang, H.e. Zheng, L. Tong, Q. Yang, J.u. Li, S.X. Mao, Size-Dependent Brittle-to-Ductile Transition in Silica Glass Nanofibers, Nano Lett. 16 (1) (2016) 105–113, https://doi.org/10.1021/acs.nanolett.5b0307010.1021/acs.nanolett.5b03070.s001.
[61] B. Mantisi, A. Tanguy, G. Kermouche, E. Barthel, Atomistic response of a model silica glass under shear and pressure, Eur. Phys. J. B. 85 (2012) 304, https://doi.org/10.1140/epjb/e2012-30317-6.
[62] P.Y. Huang, S. Kurasch, J.S. Alden, A. Shekhawat, A.A. Alemi, P.L. McEuen, J.P. Sethna, U. Kaiser, D.A. Muller, Imaging atomic rearrangements in two-dimensional silica glass: watching silica's dance, Science (80-,) 342 (6155) (2013) 224–227.
[63] Y.-C. Chen, K. Nomura, R.K. Kalia, A. Nakano, P. Vashishta, Void Deformation and Breakup in Shearing Silica Glass, Phys. Rev. Lett. 103 (2009) 35501, https://doi.org/10.1103/PhysRevLett.103.035501.
[64] Y. Zhang, L. Huang, Y. Shi, Molecular dynamics study on the viscosity of glass-forming systems near and below the glass transition temperature, J. Am. Ceram. Soc. 104 (2021) 6227–6241, https://doi.org/10.1111/jace.18006.